



3D-Printed Fe-doped silicon carbide monolithic catalysts for wet peroxide oxidation processes

A. Quintanilla^{a,*}, J.A. Casas^a, P. Miranzo^b, M.I. Osendi^b, M. Belmonte^{b,*}

^a Sección de Ingeniería Química, Universidad Autónoma de Madrid, 28049, Madrid, Spain

^b Institute of Ceramics and Glass (ICV-CSIC), 28049, Madrid, Spain



ARTICLE INFO

Keywords:

3D printing
Monolith
Silicon carbide
Robocasting
Catalytic wet peroxide oxidation

ABSTRACT

The catalyst stability has become a key issue for wet peroxide oxidation (CWPO) processes. Herein, an alternative method for the manufacturing of iron (Fe) catalysts by using three-dimensional (3D) printing techniques is proposed to enhance the Fe immobilization, where these metallic nanoparticles are part of a printable aqueous silicon carbide (SiC)-based ink. Cylindrical Fe/SiC monoliths ($D \sim 13$ mm, $H \sim 4.5$ mm, 74 squared cells cm^{-2}) are manufactured by direct ink writing (Robocasting) and further treatment up to 1500°C into a spark plasma sintering (SPS) furnace to assure a certain mechanical integrity. It was found that the increasing SPS temperature progressively decreases the porosity -or increases the apparent density- of the printed struts, lowering the accessibility of reactants to the Fe sites but improving the catalyst mechanical strength and leaching resistance. 3D Fe/SiC monoliths treated at 1200°C arise as robust catalysts for CWPO processes due to the combination of good catalytic activity, highly-efficient H_2O_2 decomposition, long-term stability and excellent mechanical strength. A simple potential kinetic model is proposed, capable of describing the phenol disappearance, TOC removal and H_2O_2 consumption. The results of this study point out a new approach for the conformation by Robocasting of metal-based catalysts in suitable morphological 3D-structures for scaling-up reactions.

1. Introduction

The treatment of the wastewater coming from industrial processes is increasingly becoming an environmental and health priority. Catalytic Wet Peroxide Oxidation (CWPO) is one of the most promising technologies to remove non-biodegradable contaminants in wastewater. CWPO operates under mild conditions (temperatures and pressures in the range of $25\text{--}100^\circ\text{C}$ and $0.1\text{--}0.5$ MPa, respectively) [1] and employs hydrogen peroxide (H_2O_2) as oxidant, which is considered an environmentally friendly agent. This process requires a solid catalyst with redox properties to generate hydroxyl ($\text{HO}\cdot$) and hydroperoxy ($\text{HOO}\cdot$) radicals from H_2O_2 decomposition. These radical species easily react with the pollutants, oxidizing them.

The catalyst par excellence is iron (Fe) due to its low cost and high-organic oxidation activity. Fe is usually anchored to different materials as iron oxide in powder or granular form, viz. alumina [2], silica [3], titania [4], zeolites [5], mesoporous molecular sieves [6], pillared clays [7] and activated carbon [8]. However, the poor resistance offered by Fe containing materials to leaching under the acidic conditions of the CWPO process is limiting its industrial application. Therefore, different approaches are being explored, among others, the employ of alternative

catalysts either metal-based ones, such as copper [9], manganese [10], cobalt [11], gold [12] or metal-free carbon catalysts [13]. When metal leaching is not significant or even null, as it is the case of carbon-based catalysts, the contribution of the homogeneous reaction is avoided and, thus, modest catalytic activities are achieved [14]. The high-cost gold nanoparticles are an exception but in spite of a high catalytic activity, they are susceptible to reversible poisoning by oxidation intermediates [15]. On the other hand, the industrial implementation of the CWPO catalysts that implies their conformation in suitable morphological characteristics with the appropriate mechanical strength remains scarcely explored and just few works can be found. In this way, Taran et al. [16] studied the wet peroxide oxidation of phenol in a flow reactor using different geometric forms (cylinders, trefoils, spheres and monoliths) and sizes of copper-doped zeolites. These authors found that the highest efficiency toward phenol destruction was observed for the catalysts with the greatest geometric surface area that corresponded to trefoils and monoliths with high channel density.

The above highly demanding requirements could be accomplished by employing additive manufacturing techniques [17] to design with a precise control of the size and shape, rigid structures with embedded catalysts adapted to the requirements of the CWPO process. Herein, we

* Corresponding authors.

E-mail addresses: asun.quintanilla@uam.es (A. Quintanilla), mbelmonte@icv.csic.es (M. Belmonte).

propose the use of cost-effective direct ink writing techniques such as robocasting [18,19] to produce three-dimensional (3D) architected ceramics by colloidal processing employing an aqueous-based ink containing the catalytic material. At present, scarce works can be found on 3D catalysts directly obtained by robocasting [20–22]. However, we expect upcoming interest in the application of this technique to the catalyst manufacturing because it can overcome the intricacies of the scale-up of heterogeneous catalyst (large sizes, scale-up formulation and structuring). The recent study by Tubio et al. [22], the only reported work up to now that focus on metal-based catalysts with a woodpile porous structure achieved by robocasting, provided promising results by demonstrating the good recyclability of these 3D printed Cu/Al₂O₃ catalysts in Ullmann reactions without leaching contamination of the reaction products.

The mechanical integrity of the 3D printed structures that allows manipulating them when using as catalysts is also an important advantage. Although that integrity should increase with the density of the scaffold [23], at the same time, it could compromise their catalytic activity by decreasing the porosity and, hence, the number of available catalytic active sites.

This work will accomplish the robocasting of 3D Fe/silicon carbide (SiC) catalysts by architecting colloidal suspensions of Fe-doped (0.52 wt.%) SiC powders into porous monoliths. SiC is selected as the catalyst support due to its excellent corrosion resistance to most chemicals, in addition to other attractive properties like low density, good thermal stability and high strength [24,25]. The challenge in the fabrication of this 3D Fe incorporated monoliths for the CWPO process is to trade-off a good catalytic properties (activity and stability) –promoted by the embedded Fe active sites accessible in the SiC porous structure– and a certain mechanical strength. Both requirements could be met by tailoring the porosity of the solid structure through heat treatments of the SiC support at temperatures that only produce a partial sintering, presently from 1000 to 1500 °C in a spark plasma furnace. The catalytic activity and stability of Fe/SiC monoliths thus obtained are studied in the CWPO of phenol, a common pollutant in wastewaters [26]. The results describing the effect of process variables including temperature, initial phenol, total organic carbon (TOC) and H₂O₂ concentrations are modelled according to some proposed reaction kinetics. The effect of mass transfer limitation on the CWPO of phenol is also reported. To the best of our knowledge, no reports can be found on 3D printed catalyst for CWPO reactions hitherto.

2. Experimental

2.1. Monolith fabrication

Nanosized β-SiC powders containing 0.52 wt.% of Fe (Nanostructured & Amorphous Materials Inc. -NanoAmor-, polytype 3 C with mean SiC particle size of 45–55 nm) were employed as starting material. The apparent viscosity (η) and the shear storage (G') and loss (G'') moduli of the Fe/SiC inks were determined with a rheometer (CVO 100 D, Bohlin Instruments) equipped with a cone-and-plate geometry (diameter: 40 mm; cone angle: 4°). For η , the shear stress (τ) was recorded as shear rate ($\dot{\gamma}$) was increased from 0.0878–200 s⁻¹. For G' and G'' data, oscillation measurements were performed at a frequency of 1 Hz and ascending stress sweep from 0.5 to 1000 Pa. In order to develop printable Fe/SiC inks, we used as starting point a previous reported study on SiC-based inks containing oxide sintering additives [27]. Therefore, for the current Fe/SiC ink composition (no sintering aids), the solids, deionized water and organics contents were readjusted to get the required pseudoplastic behaviour, sequentially adding to deionized water the following materials: 55.7 wt.% of Fe/SiC, 3.7 wt.% of high molecular weight polyethylenimine (H-PEI, PEI 25000, Sigma Aldrich; < 1 wt.% of water content), 3.8 wt.% of low molecular weight polyethylenimine (L-PEI, PEI 2000, Sigma Aldrich; 50 wt.% of water content), 7.0 wt.% of hydroxypropyl methylcellulose (MC, Methocel

F4M, Dow Chemical Co.; 95 wt.% of water content). After each addition, the ink was homogenized by planetary centrifugal mixing (ARE-250, Thinky Company) at 2000 r.p.m. for 30–60 s. 3D cylindrical Fe/SiC periodic lattices were computer designed (RoboCAD 4.0, 3-D Inks LLC) and reproduced at room temperature onto an alumina substrate with a custom three-axis robocasting system (A-3200, 3-D Inks LLC) using tips with inner diameter of 330 µm. The ink extrusion speed was automatically controlled to keep a constant volumetric flow rate of 0.25πD²v, where D is the inner diameter of the nozzle and v is the X-Y table velocity set at 25 mm s⁻¹. The as-printed scaffolds were heat treated at 600 °C in air for 2 h to completely burn-out the organics employed for the ink formulation, according to the thermogravimetric analysis (Fig. S1, Supporting information), and were employed as reference catalyst (labelled as REFERENCE). Some of these scaffolds were further pressureless sintered into a spark plasma sintering furnace (SPS, SPS-510CE; Fuji Electronic Industrial Co., Ltd) to induce differences of density, i.e. porosity, in the structures, looking for a convenient balance between the CWPO performance and the adequate strength. The heat treatments were carried out in an argon atmosphere (~ 6 kPa) at temperatures ranging from 1000 to 1500 °C, holding for 5 min at the set temperature. The resulting monoliths are labelled as SPS-1000, SPS-1200 and SPS-1500 referring to the corresponding treatment temperatures.

2.2. Structure characterization

Total porosity (ϵ) was determined as the sum of the macro-porosity due to the patterned design and the micro-porosity of the ceramic struts, estimated by the Archimedes' method using distilled water as the immersion medium. The apparent density (ρ_p) of the monoliths correspond to the mass of Fe/SiC catalyst per volume occupied by the solid struts. Fracture surfaces of struts were observed with a field emission scanning electron microscope (FESEM; Hitachi S-4700). Median grain diameter (d_{50}) of the SiC support as a function of the SPS treatment was estimated by imaging analysis methods on FESEM images considering at least 700 features. Specific surface area was obtained in a Micromeritics Tristar 3000 apparatus. The overall Fe content (fresh and used) in the monoliths was determined by total reflection X-ray fluorescence (TXRF EXTRA II, Rich & Seifert), using Si-Li detector in a TXRF Extra-II spectrometer. Transmission electron microscopy (TEM) images were taken on mortar crushed specimens with a JOEL JEM 2100 at an accelerating voltage of 200 kV. X-ray photoelectron spectroscopy (XPS) analysis was carried out using a Physical Electronics (mod. ESCA 5701) equipped with a monochromatic Mg Ka X-ray excitation source. The binding energies in the Fe 2p spectra were calibrated by setting C1s at 284.6 eV.

2.3. Mechanical characterization

3D Fe/SiC scaffolds were compression tested using a universal testing machine (ZwickiLine Z5.0 TS, Zwick-Roell) and a displacement rate of 0.5 mm min⁻¹ until crushing. The robocast specimens were previously ground at the top/bottom surfaces to assure a homogenous distribution of the load on the whole 3D structure. Stress and strain values were determined from the load and displacement data, and the compressive strength was calculated from the load at failure and the nominal contact surface area.

2.4. CWPO experiments

The catalytic activity of the different Fe/SiC monoliths, *viz.* REFERENCE, SPS-1000, SPS-1200 and SPS-1500, for the CWPO of phenol was studied in a tubular double jacket glass reactor ($d_i = 15$ mm) operated in up-flow mode and loaded with three monolithic pieces (total weight, W = 0.93 g). The runs were conducted at $[Phenol]_0 = 1$ g L⁻¹, $[H_2O_2]_0 = 5$ g L⁻¹, natural pH₀, T = 75 °C, residence time

$(t_r) = 0\text{--}10\text{ min}$ and space time (τ) = $0\text{--}130\text{ g}_{\text{CAT}}\text{ h L}^{-1}$. Control experiments in absence of catalyst, with the original β -SiC commercial nanoparticles and alternatively with β -SiC nanoparticles with just traces of Fe (0.05 wt.%) were performed at the same operating conditions. The latter nanoparticles resulted from the washing of the as-received β -SiC commercial nanoparticles, typically 2.5 g of SiC in 250 mL of HCl (37%) for 24 h under vigorous stirring at room temperature.

The long-term stability of the SPS-1200 monoliths was tested in a reactor loaded with nine cylindrical pieces ($W = 2.83\text{ g}$) at the above selected conditions for CWPO performance and at two flow rates, 0.5 and 0.125 mL min^{-1} , corresponding with $\tau = 94$ and $378\text{ g}_{\text{CAT}}\text{ h L}^{-1}$ or $t_r = 6$ and 24 min, respectively. Further kinetic experiments were carried out over a wide range of operating conditions: $[\text{Phenol}]_0 = 0.5\text{--}5\text{ g L}^{-1}$, $[\text{H}_2\text{O}_2]_0 = 2.5\text{--}6.5\text{ g L}^{-1}$, $T = 65\text{--}85^\circ\text{C}$ and $\tau = 0\text{--}378\text{ g}_{\text{CAT}}\text{ h L}^{-1}$.

2.5. Analytical methods

Liquid samples from the reactor were analyzed by different procedures. Phenol and aromatic by-products were determined by high performance liquid chromatography (HPLC, Varian, Mod. ProStar, PDA detector with a 5 μm FORTIS C18 column $150 \times 4.6\text{ mm}$); whereas TOC was estimated using a specific analyzer (Shimadzu TOC VSCH). H_2O_2 concentration was determined by employing the TiOSO_4 method. The content of Fe in solution was measured by colorimetric test with an ORBEKO -Hellige MC500 Colorimeter and, in some samples, also confirmed by TXRF.

3. Results and discussion

3.1. Fabrication and characterization of Fe/SiC monoliths

The manufacturing process of the Fe/SiC scaffolds first required the development of a printable ink, which must exhibit an adequate pseudoplastoelastic behaviour. To achieve this goal, different organic additives were sequentially added to an Fe/SiC containing aqueous ink, starting with H-PEI and L-PEI that were employed as dispersant agents to improve the solids content, followed by the addition of MC as viscosifying agent. The ink composition was formed by 38.3 wt.% of deionized water, 55.7 wt.% of Fe/SiC, and 6.0 wt.% of organics (62.5, 28.2, and 9.3 in vol.%, respectively). The resulting ink presented a shear thinning behaviour, as it was confirmed by the decrease of several orders of magnitude of the apparent viscosity as the shear rate augmented from 10^{-1} to 10^2 s^{-1} (Fig. 1a). This response allowed printing low viscous ($\eta = 6\text{--}10\text{ Pa s}$) Fe/SiC ceramic filaments through the fine tip (330 μm inner diameter) in the shear rate region of $30\text{--}70\text{ s}^{-1}$, and retaining their shape once printed because the abrupt increase in viscosity ($> 10^4\text{ Pa s}$) after setting. In addition, the ink exhibited (Fig. 1b) both high storage modulus ($G' \sim 5 \times 10^4\text{ Pa}$) and yield stress ($\tau_y \sim 10^3\text{ Pa}$) -defined by the point where G'' (loss modulus) equals to G' which facilitated retaining the filamentary shape and avoided the collapse of the built 3D structures. Cylindrical Fe/SiC periodic scaffolds of $\sim 13\text{ mm}$ of diameter and $\sim 4.5\text{ mm}$ of height (20 filament layers) with a spanned distance between the filaments in the linear array of $\sim 1.3\text{ mm}$ were computer-aided designed (Fig. 1c). The monoliths contain 74 square cells per cm^2 . A real size photo is shown in Fig. 1d.

Table 1 collects the apparent density and the total porosity of the REFERENCE and the scaffolds sintered at different temperatures. As sintering additives were not added to the SiC powders, densification was mostly inhibited. The ρ_p values of the monoliths increasing from 1.13 g cm^{-3} (REFERENCE) up to 1.72 g cm^{-3} (SPS-1500), which constitutes an increment in the density of $\sim 50\%$ with the 1500°C SPS treatment but it is far from the theoretical density of $\text{SiC} = 3.22\text{ g cm}^{-3}$. Conversely, as expected, ε_b , taken as the sum of the macro-porosity due to the patterned design and the micro-porosity of the ceramic struts, decreased from 70.0% (REFERENCE) to 65.6% (SPS-

1500), diminishing the surface area (S_{BET}) as well (Table 1). The dimensions of the cylindrical Fe/SiC monoliths are: $D \sim 13\text{ mm}$, $H \sim 4.5\text{ mm}$, $D_{\text{open}} \sim 0.9\text{ mm}$ and $\delta_w = 0.26\text{ cm}$.

As an example, Fig. 2a shows a representative image of the fracture surface of one of the monoliths, in particular, the SPS-1200 one, where the retention of the 3D architecture is clearly visible. The analysis of the microstructure of the ceramic struts (Fig. 2b) revealed that the mean particle size of SiC was in the range of 39–46 nm for all monoliths independently of the SPS treatment, value that was also similar to the particle size of the original powders (45 nm).

Regarding the active catalytic phase, the Fe content remained invariable for all the monoliths, i.e. $0.52 \pm 0.03\text{ wt.}\%$, with a diameter of $12.7 \pm 4.5\text{ nm}$ for the isolated spherical Fe nanoparticles as determined by the TEM images (Fig. 2c). Besides, the surface content of Fe and its oxidation state in the struts for the different SPSed monoliths was determined by analysing of the XPS signal in the Fe 2p region. The spectrum of the REFERENCE sample is provided in Fig. 2d as representative example. Two main peaks located at 710.6 and 723.0 eV were clearly observed and ascribed to $\text{Fe } 2p_{3/2}$ and $2p_{1/2}$ cationic species, respectively [28]. The two satellite peaks located at energy values c.a. 3.5 and 7.6 eV higher than the corresponding main peaks (Fig. 2d) corresponded to Fe^{2+} and Fe^{3+} , respectively. The same cationic Fe species were detected for the SPSed monoliths (Fig. S2 of the Supporting information shows the spectrum recorded for SPS-1500). Both ionic states of Fe are catalytically active in the decomposition of H_2O_2 [29]. The overall Fe content on the outermost surface of the SiC scaffold calculated from the deconvolution of the main XPS peaks is collected in Table 1. While for the REFERENCE material that content was 0.33 wt.%, it considerably decreased (30–40% reduction) for the SPSed monoliths.

3.2. CWPO performance

First, it was verified that liquid-phase reaction (in absence of catalyst) was not competitive with the catalysts. Furthermore, the Fe/SiC raw powders exhibited a high catalytic activity. Conversions of phenol and TOC of 100 and 60%, respectively, were achieved at $7.8\text{ g}_{\text{cat}}\text{ h L}^{-1}$ and 1 h of residence time, due to the contribution of the significant leached Fe content -8.3 ppm- to the reaction [30–32]. On the other hand, the powders became inactive once washed with a strong acid (Fe content within the SiC powders dropped to 0.05 wt.%), which evidenced that the catalytic activity is clearly associated to Fe without contribution of the SiC nanoparticles.

When the different Fe/SiC monoliths were used in the CWPO reaction, the initial exposure to the reacting stream triggered the leaching of the most liable Fe during approximately 30 h on stream, reaching, afterwards, a stable stage where the Fe content in the effluents became insignificant. The Fe leachability decreased with the SPS temperature (see values of $\text{Fe}_{\text{leached}}$ in Table 1), from 18.5 (REFERENCE) to 5.2 wt.% (SPS-1500). These results reflect a lower availability of the Fe active sites for the catalytic reaction as the temperature increased, also confirmed by the XPS spectra (Fe_{XPS} data in Table 1).

The results obtained in the CWPO of phenol for all monoliths are shown in Fig. 3. Fe leaching was negligible in all the experiments because profiles were obtained after 30 h on-stream catalysts. As it can be seen, distinct conversion (X) profiles of phenol (Fig. 3a) and TOC (Fig. 3b) vs. space time (τ) are obtained. Note the poor mineralization achieved at the low space times employed at the reaction temperature of 75°C . This is due to the presence of oligomeric by-products (responsible of the brownish colour of the effluent) which are more refractory to the oxidation than phenol [33]. These first oxidation intermediates will preferentially remain in the liquid phase than adsorbed on the monoliths surface due to its low specific surface area (Table 1), leading to a negative repercussion in the TOC conversion. Therefore, more severe operating conditions will be required to enhance the mineralization degree, as it will be further demonstrated. Fig. 3c

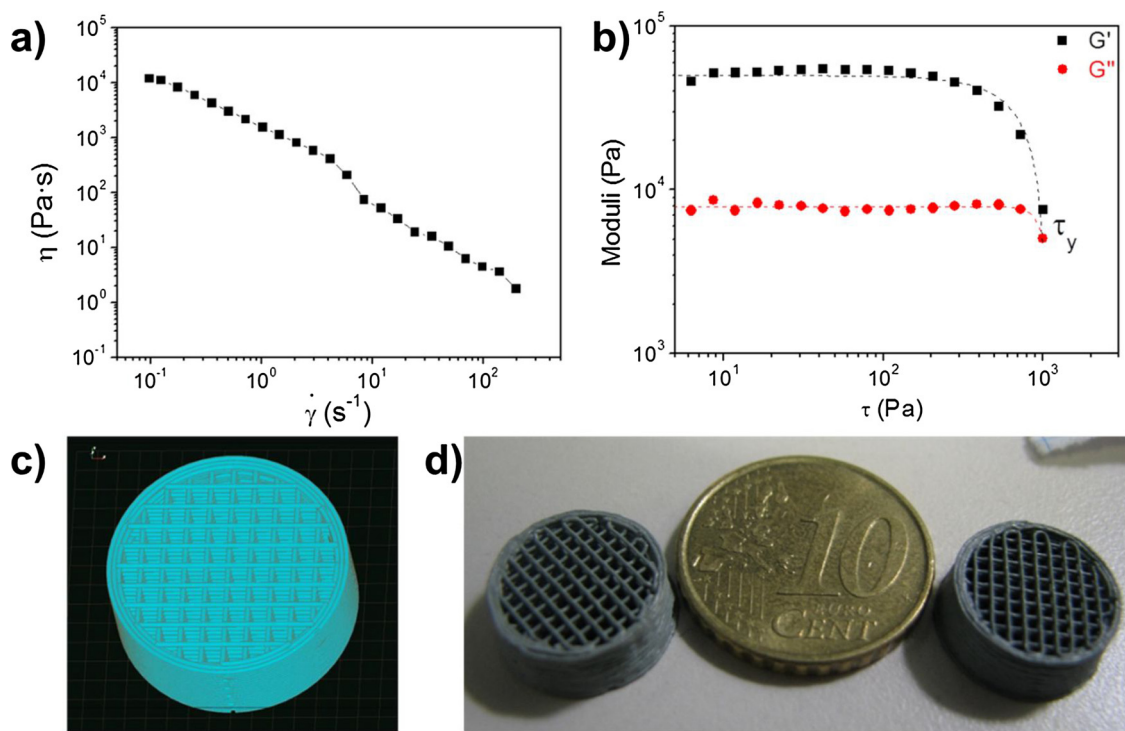


Fig. 1. Rheological behaviour of Fe/SiC-based inks and 3D printed scaffolds. a) Apparent viscosity (η) versus shear rate ($\dot{\gamma}$) and b) storage (G') and loss (G'') moduli versus shear stress (τ) for the SiC-based ink. c) CAD patterned structure and d) examples of 3D cylindrical Fe/SiC scaffolds after the burning-out process (reference material, REFERENCE) comparing their sizes with a coin of 10 euro cents.

Table 1

Characterization of 3D printed Fe/SiC monoliths as a function of the SPS temperature: apparent density (ρ_p), total porosity (ε_t), specific surface area (S_{BET}), the outermost surface Fe content from XPS spectra (Fe_{XPS}), and Fe leached after 30 h of stream determined by TXFR ($Fe_{leached}$). The reference monoliths (REFERENCE) have also been included for comparison purposes.

Monoliths	SPS temperature (°C)	ρ_p (g cm ⁻³)	ε_t (vol.%)	S_{BET} (m ² g ⁻¹)	Fe_{XPS} (wt.%)	$Fe_{leached}$ 30 h (wt.%)
REFERENCE	–	1.13	70.0	30.9	0.33	18.5
SPS-1000	1000	1.44	68.9	29.4	0.23	11.0
SPS-1200	1200	1.51	67.3	23.5	0.22	10.1
SPS-1500	1500	1.72	65.6	22.0	0.20	5.2

illustrates the effect of the heat treatment on the apparent kinetic constants (k_{app}) calculated assuming a pseudo-first order kinetic reaction. k_{app} progressively diminished with the SPS temperature up to 1200 °C and, then, more abruptly for the 1500 °C treatment, observing for this latter 3D catalyst a reduction of activity with respect to the REFERENCE monolith of 50 and 70% for phenol disappearance and TOC removal, respectively. Considering that the k_{app} values do not correlate with the remaining Fe content (lower in the SPS-1000 than SPS-1500, as indicated in Fig. 3c), it seems reasonable to attribute the differences in the catalytic behaviour of the monoliths to a lower accessibility of the Fe active sites to reactants, which is caused by the decrease in ε_t or the increase in ρ_p (Table 1). Fe/SiC monoliths also worked as efficient catalysts in the decomposition of H₂O₂ into radical species, as it can be seen in Fig. 3 d where TOC vs. H₂O₂ conversions are depicted. The consumption of H₂O₂ is equivalent to TOC abatement, which indicates that the radical species formed, HO· and HOO·, reacted with the organic compounds (phenol and by-product species) instead of being consumed in spurious parasite reactions. The selected SPS temperature studied have no influence on the catalyst H₂O₂-efficiency, at least within the levels of TOC removal here achieved. Due to the poor activity achieved by the SPS-1500 monoliths, they were not considered for further experiments.

In addition to a good catalytic behaviour, the monoliths should also exhibit an adequate mechanical integrity for their manipulation under service conditions. Then, compression tests were performed for REFERENCE, SPS-1000 and SPS-1200 monoliths and representative examples of their stress-strain curves are collected in Fig. 4a. All the scaffolds initially presented a linear elastic region that extended until reaching the maximum stress value (compressive strength, σ). Within this elastic region, the beams in Fe/SiC cells progressively bent and fractured until the scaffold collapsed. As the ρ_p of the scaffolds augmented, larger crushing strengths, σ , were attained (Fig. 4b). In fact, σ increases by 120% when comparing the REFERENCE monoliths ($\rho_p = 1.13$ g cm⁻³, $\sigma = 1.6$ MPa) to the SPS-1200 ones ($\rho_p = 1.51$ g cm⁻³, $\sigma = 3.5$ MPa), following parabolic trend with density. This increment in σ was also accompanied by higher strains (~30%) of the structure at fracture. The stress-strain curves showed a slow drop of the stress after the maximum σ value was attained (Fig. 4a), indicating of certain load bearing capability of the structure instead of a catastrophic failure. This behaviour is linked to the progressive collapse of the Fe/SiC cells that produced the gradual fracture of the monoliths.

According to the above results, the SPS-1200 monoliths arise as the best option to balance both reasonable mechanical strength and good

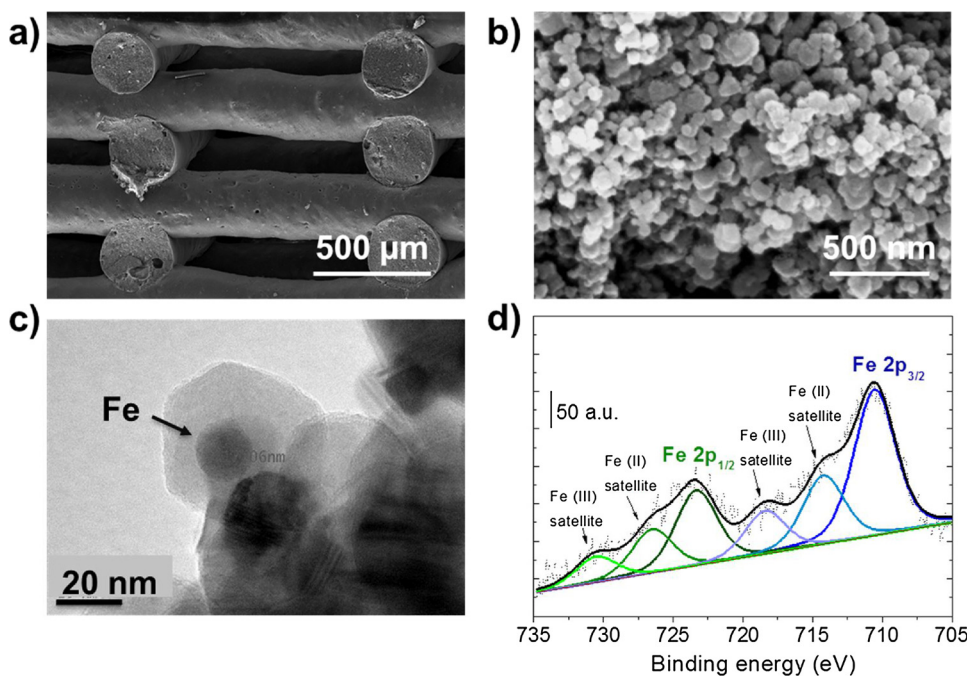


Fig. 2. a) FESEM micrographs showing a cross section of a scaffold showing the woodpile arrangement and b) typical microstructure of nanosized SiC grains inside the strut and c) TEM image of SPS-1200 showing an embedded Fe particle, and d) XPS spectrum and deconvolution of Fe 2p peaks of the reference sample.

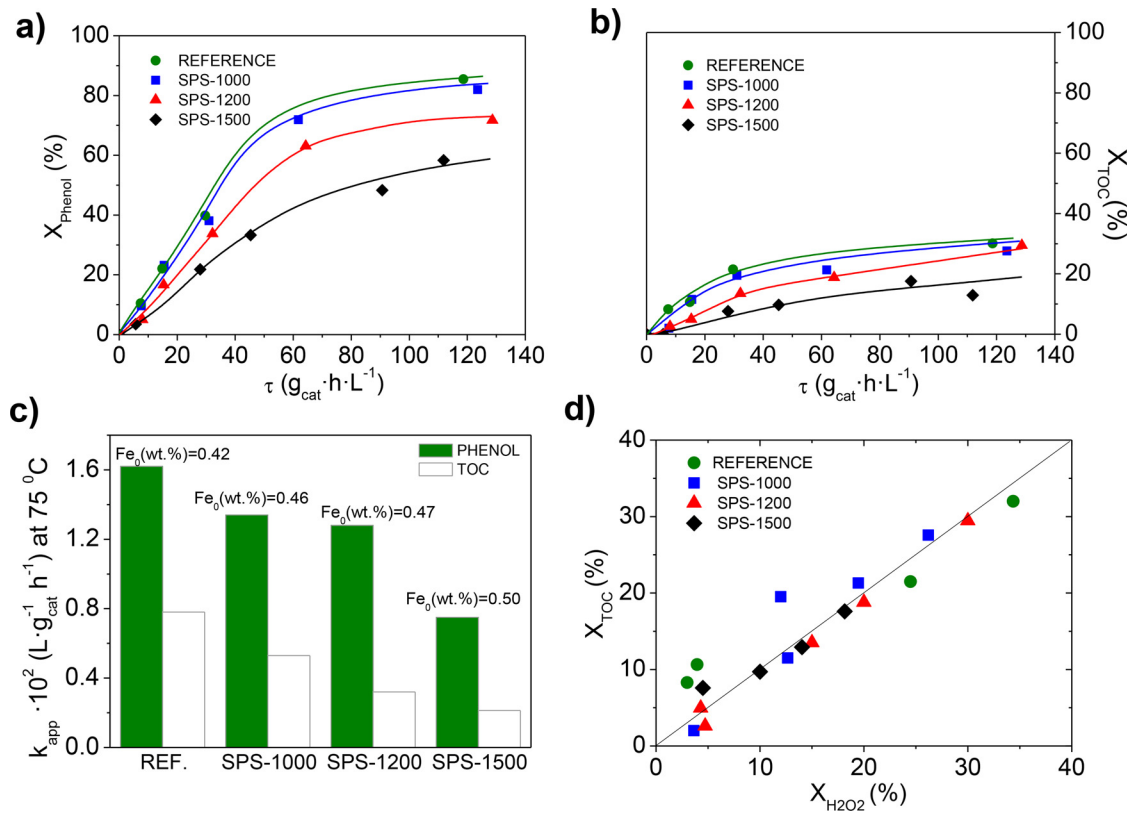


Fig. 3. Conversions (X) profiles of a) phenol and b) TOC, c) apparent kinetic constants (k_{app}) of phenol disappearance and TOC removal as a function of the SPS temperature, d) efficiency in the H_2O_2 -consumption in presence of 3D-printed Fe/SiC monoliths. Operating conditions: $[Phenol]_0 = 1 \text{ g L}^{-1}$, $[H_2O_2]_0 = 5 \text{ g L}^{-1}$, natural pH_0 , $T = 75 \text{ }^\circ\text{C}$, $t_r = 0\text{--}10 \text{ min}$.

catalytic activity in CWPO reactions. Next, a deep insight into the CWPO over these selected monoliths will be carried out by testing the operational stability in long-term use and obtaining the kinetic model for the CWPO of phenol that can be very useful for optimizing process conditions.

3.3. Catalyst stability

The key point in the application of novel heterogeneous catalysts in CWPO is the stability with time-on-stream, which could be questionable due to the amount of active Fe initially lost by leaching (Table 1). A

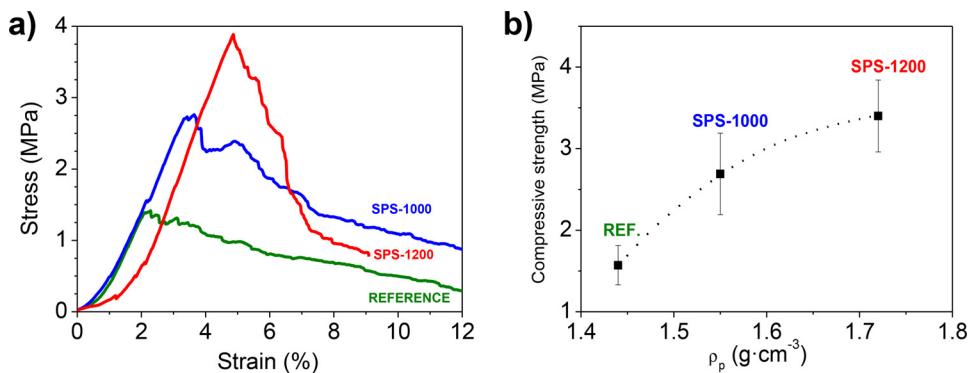


Fig. 4. Mechanical resistance of the monoliths. a) Representative stress-strain curves for the REFERENCE, SPS-1000 and SPS-1200 scaffolds, and b) compressive strength (σ) versus the apparent density (ρ_p).

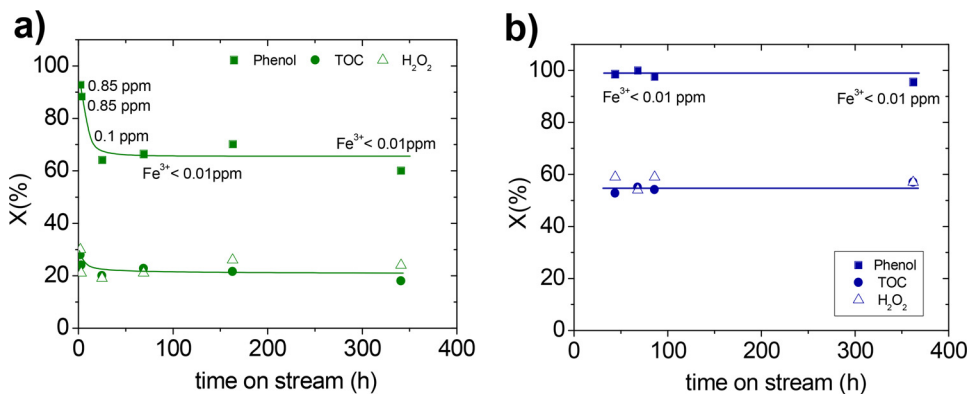


Fig. 5. Long-term runs of SPS-1200 Fe/Si monoliths tested at 75 °C at: a) 378 and b) 94.4 $\text{g}_{\text{cat}} \cdot \text{h} \cdot \text{L}^{-1}$.

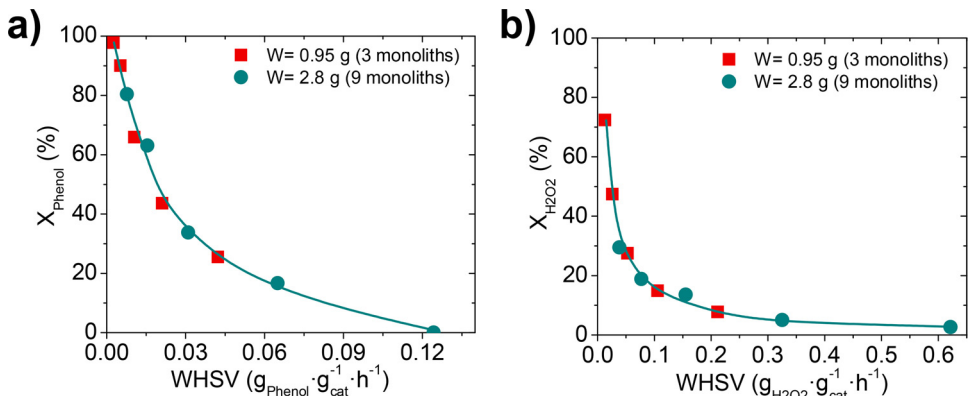


Fig. 6. a) Phenol conversion (X_{phenol}) vs. WHSV, b) H_2O_2 conversion ($X_{\text{H}_2\text{O}_2}$) vs. WHSV.

reactor loaded with nine cylindrical SPS-1200 monoliths ($W = 2.83 \text{ g}$) was used to perform the long-term operation at large space-times, $\tau = 94.4$ and $378 \text{ g}_{\text{cat}} \cdot \text{h} \cdot \text{L}^{-1}$. The constant values of phenol, TOC and H_2O_2 conversions with time on stream (Fig. 5) evidenced that the SPS-1200 catalyst exhibits an excellent stability with no apparent deactivation for 350 h on stream once overpassed the initial period of 20 h, when Fe was leached out. As it can be seen, with Fe concentrations as low as 0.1 ppm, the homogeneous contribution to the overall phenol uptake was negligible and the activity remained constant.

Furthermore, after 350 h of catalytic reaction, the monoliths were thermogravimetric analysed (Fig. S3, Supporting information) and compared with the fresh ones (not used). The results evidenced that in the case of used monoliths, a slight weight loss was observed at temperature over 350 °C which is associated to the burn out process of the species adsorbed on the monolith surface after the catalytic reactions,

in particular, oligomers products [34]. Note that the amount of oligomers deposited on the monolith surface remained very low ($\sim 0.2 \text{ wt\%}$) and, hence, the activity was not affected. Both monoliths exhibited an increase in their weights above 600 °C that is linked to the progressive SiC oxidation of the scaffolds.

3.4. Mass transfer analysis and kinetic modelling

The existence of external mass transfer limitation must be previously verified by experimentation. The liquid solid mass transfer coefficients of reactants cannot be estimated by the existing correlations for monolith reactors [35] because the flow pattern inside the monolith channel during the CWPO reaction is unpredictable. Besides, the flow is changeable along the length of the channel due to the progressive mineralization of phenol and oxidized intermediates that results in the

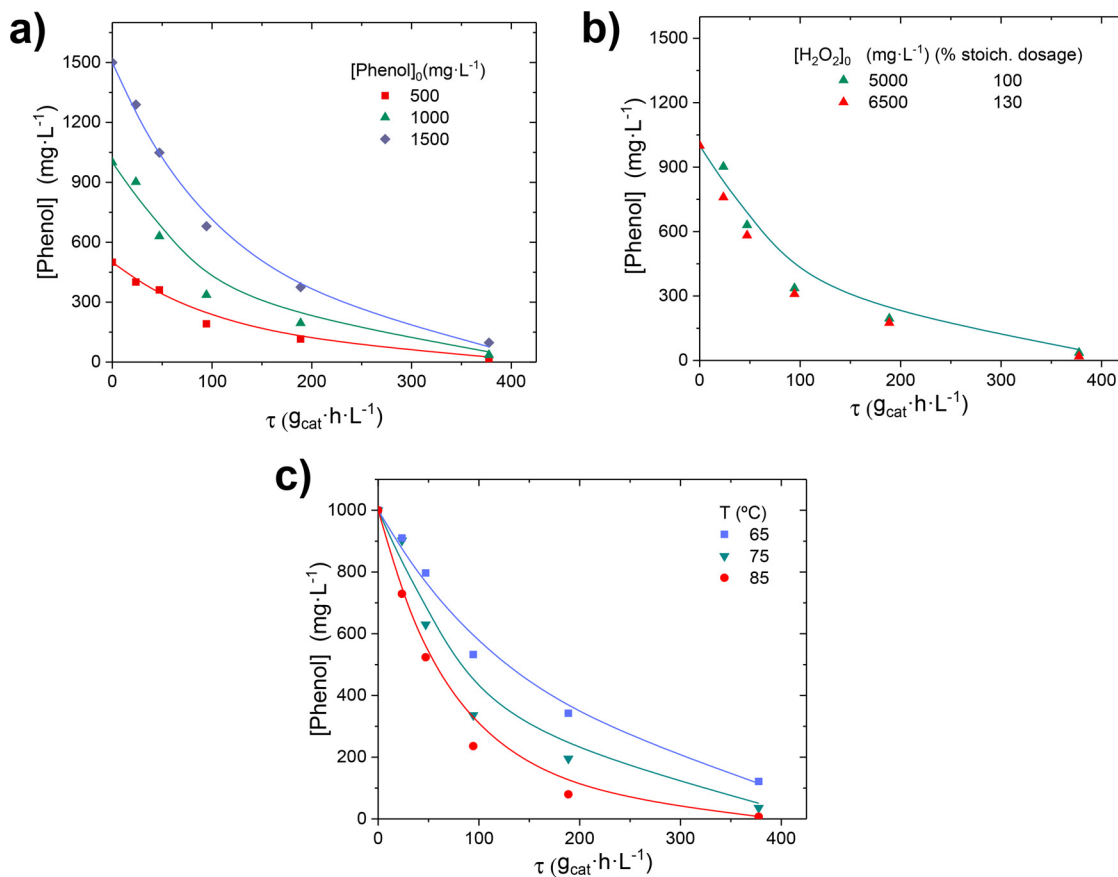


Fig. 7. Experimental (symbols) and predicted (curves) time-course of phenol concentration under different operating conditions.

generation of volatile compounds such as CO₂ and CO [32]. Thus, the external mass transfer limitation was experimentally verified by studying the effect of the liquid flow rate ($Q_L = 0.125\text{--}2 \text{ mL}\cdot\text{min}^{-1}$) on phenol and H₂O₂ conversions (Figs. 6a and b, respectively) within a similar range of weight hour space velocity (WHSV = reactant mass flow/mass of catalyst), calculated as $Q_L[\text{Phenol or H}_2\text{O}_2]_0\text{W}^{-1}$, in g_{phenol} or H₂O₂·g_{cat}⁻¹·h⁻¹). The experiments were performed in reactors of two different lengths loaded with three and nine monolith structures, the amount of catalyst being 0.95 and 2.83 g, respectively. The liquid flow rate was proportionally changed to the reactor length to keep the WHSV constant. Figs. 6a,b show that phenol and H₂O₂ conversions data vs. WHSV in both reactors show the same profile at similar conditions of temperature and reactant concentrations, indicating that external mass transfer limitations can be neglected.

Within the above liquid flow rate range, the oxidation experiments were then performed at different operating conditions for initial phenol concentrations (500–1500 mg L⁻¹), H₂O₂ dosages (100–130% stoich. dosage) and temperatures (65–85 °C) in the reactor loaded with 2.83 g of SPS-1200 monoliths. The effect of each variable on phenol (Fig. 7), TOC (Fig. 8) and H₂O₂ (Fig. 9) concentrations at the reactor outlet was studied as a function of τ by keeping all other variables constant. Interestingly, at the most severe conditions, 85 °C and 378 g_{CAT} h L⁻¹ (equivalent to a $t_r = 36$ min), complete phenol disappearance, 70% TOC removal and 72% H₂O₂ consumption were achieved using the typical inlet effluent in CWPO studies (1 g L⁻¹ of phenol solution and the stoichiometric dosage of H₂O₂).

Different models were proposed to fit by nonlinear regression to the experimental data of Figs. 7, 8 and 9. The numerical integration of the rate equations, assuming isothermal plug-flow inside the channel, was solved at each temperature with the Microsoft Excel Solver (Microsoft Office 2010, MicrosoftCorp.) based on the Generalized Reduced Gradient (GRG) algorithm for least squares minimization. The pre-

exponential factors and activation energies were estimated by the Arrhenius equation. The following power-law kinetic expressions are the best fitting to the experimental data:

$$(-r_{\text{PHENOL}})\left(\frac{\text{mg PHENOL}}{\text{g}_{\text{cat}}\cdot\text{h}}\right) = 1.05\cdot 10^4 \cdot e^{-\frac{4885\pm673}{T}} \cdot C_{\text{phenol}} \quad (1)$$

$$(-r_{\text{TOC}})\left(\frac{\text{mg CARBON}}{\text{g}_{\text{cat}}\cdot\text{h}}\right) = 5.32\cdot 10^6 \cdot e^{-\frac{9724\pm62}{T}} \cdot C_{\text{TOC}}^2 \quad (2)$$

$$(-r_{\text{H}_2\text{O}_2})\left(\frac{\text{mg H}_2\text{O}_2}{\text{g}_{\text{cat}}\cdot\text{h}}\right) = 1.83\cdot 10^5 \cdot e^{-\frac{6263\pm2016}{T}} \cdot C_{\text{H}_2\text{O}_2} \quad (3)$$

The predicted concentration vs. τ profiles calculated from the discriminated model, Eqs. (1)–(3), have been included in Figs. 7–9. The parity plots shown in Fig. S4 of the Supporting information also illustrate the validation of this model. Power-law kinetics have been commonly reported in CWPO processes over different catalysts [15,33,36,37].

Herein, phenol disappearance and H₂O₂ consumption rates follow first-order kinetics, while a second order is obtained for TOC, species that lump all the organic compounds present in the liquid phase. Note from Figs. 7b and Figure 8b that phenol disappearance and TOC removal rates do not depend on H₂O₂ concentration. It is usually considered that concentration of the radical species HO[·] and HOO[·] is constant and, therefore, they can be included in the kinetic constant.

To determine whether the rate reactions are limited by the internal diffusion of the reactants along the wall thickness of the channels ($\delta_w = 0.026$ cm), the internal effectiveness factor in the phenol disappearance and H₂O₂ decomposition reactions (η_{phenol} and $\eta_{\text{H}_2\text{O}_2}$, respectively) were estimated at three reaction temperatures, 65, 75 and 85 °C, as a function of the Thiele Modulus (φ):

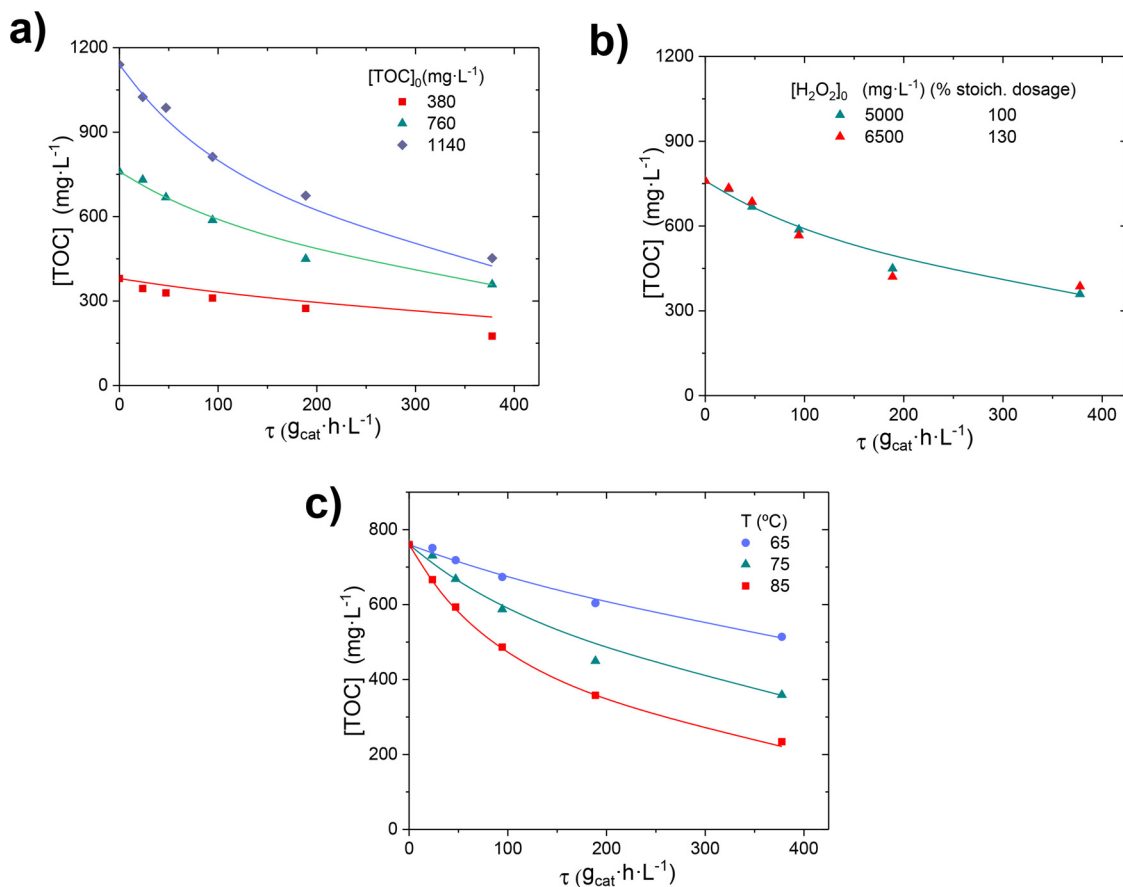


Fig. 8. Experimental (symbols) and predicted (curves) time-course of TOC concentration under different operating conditions.

$$\phi = L \cdot \sqrt{\frac{k_v}{D_{\text{eff}}}} \quad (4)$$

in which the characteristic length, L , is equal to half of the δ_w (in cm), k_v is the observed kinetic constant (s^{-1}) of Eqs. (1) and (3) and D_{eff} is effective diffusivity ($cm^2 s^{-1}$) calculated from the molecular diffusion of each of reactant in water, with a tortuosity factor assumed to be 2 and a particle porosity equal to 0.13. The molecular diffusion of phenol and H_2O_2 in water was estimated using the Wilke-Chang correlation [38]. The values of molecular diffusion and effective diffusivity for both the phenol as well as the H_2O_2 at the different temperatures are given in Table S1 of the Supporting information.

The internal effectiveness factor values for phenol and H_2O_2 as a function of the wall thickness are shown in Figs. 10a and b, respectively. Applying the Wheeler-Weisz (Φ) criteria ($\Phi = \eta \varphi^2 < 0.15$) to evaluate the absence of the internal diffusion limitation, it can be seen that the wall diffusion limitation of H_2O_2 is neglected. Meanwhile, phenol disappearance rate is somehow diffusion-limited at temperatures from 75 °C. η_{phenol} values of 0.94 and 0.92 should be considered for the estimation of the intrinsic kinetic constants at 75 and 85 °C, respectively (Fig. 10a).

4. Conclusions

The feasibility of the robocasting method for fabricating robust 3D Fe/SiC monolithic catalysts for CWPO processes using pseudoplastic Fe-doped SiC inks is demonstrated. This cost-effective method fully integrates the Fe catalyst into the ceramic scaffold and by further heat

treatments, porosity (or apparent density) of the 3D structures can be tuned, thus modifying the access of the reactants to the Fe sites. The decrease of the porosity with temperature produces a detrimental effect in the catalytic activity but a noticeable resistant to Fe leaching, hence, the intermediate temperature treatment was the most effective.

Accordingly, Fe/SiC monoliths treated at 1200 °C are promising catalysts for the treatment of wastewater by CWPO because they combine a high catalytic activity and efficiency in the H_2O_2 decomposition, good long-term stability (upon 350 h on stream) and excellent mechanical strength (3.5 MPa). The kinetic model adequately describes the target pollutant degradation (phenol), TOC removal and H_2O_2 consumption by a set of potential equations with different reaction orders (first order for phenol and H_2O_2 , and second for TOC). Some phenol internal diffusion limitation ($\eta_{\text{phenol}} = 0.94$) needs to be considered from a reaction temperature of 75 °C.

The results of this study open new perspectives in the reactor engineering solution for catalytic wastewater treatments through the design and printing of monolithic structured reactors for CWPO processes. Robocasting is presented as one-step process for the development of metal-based catalysts in suitable morphological structures for scaling-up reactions.

Acknowledgments

This work was supported by the following projects: MAT2015-67437-R (MINECO, FEDER, UE) and CTM2016-76454-R (MINECO). The authors thank Dr. Daniel Gamarra for their help in the characterization studies by XPS.

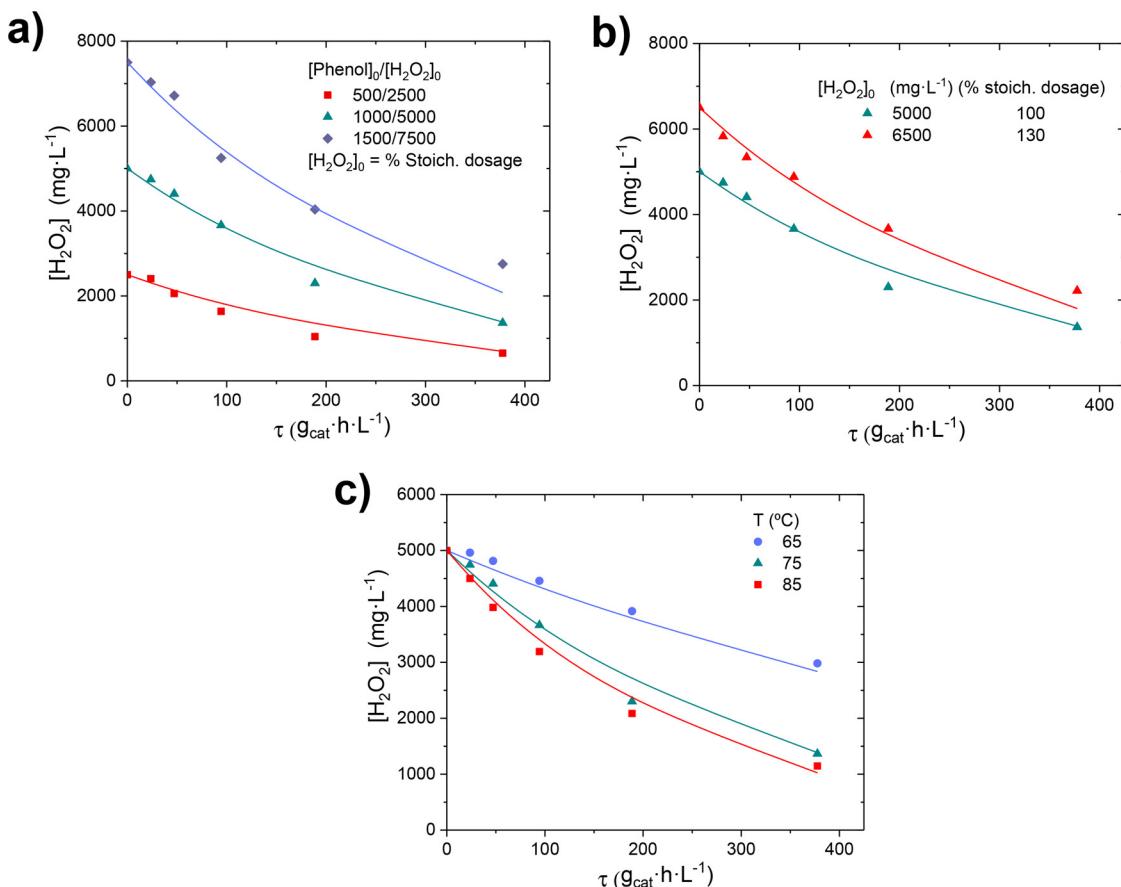


Fig. 9. Experimental (symbols) and predicted (curves) time-course of TOC concentration under different operating conditions.

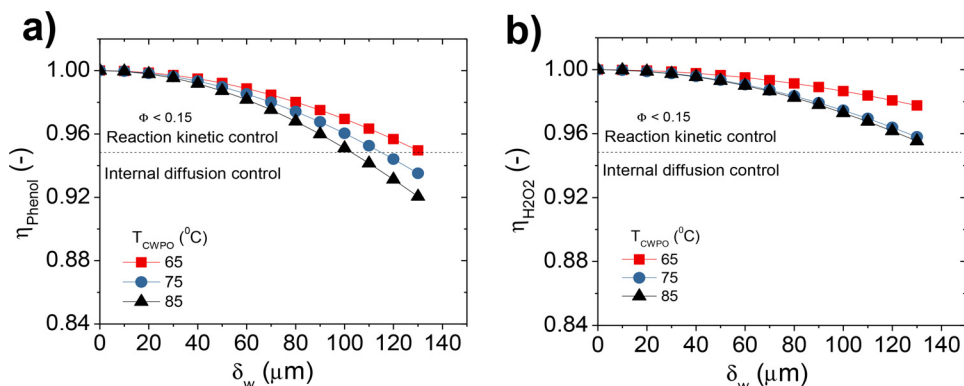


Fig. 10. a) Internal mass transfer effectiveness factor for phenol (η_{phenol}) and b) H₂O₂ (η_{H2O2}) as a function of the channel wall thickness of the SPS-1200 Fe/SiC monoliths at different CWPO temperatures.

Appendix A. Supplementary data

Supplementary material related to this article can be found, in the online version, at doi:<https://doi.org/10.1016/j.apcatb.2018.04.066>.

References

- [1] G. Pliego, J.A. Zazo, P. García-Muñoz, J.A. Casas, J.J. Rodríguez, Intensification of the Fenton process by increasing the temperature, Crit. Rev. Env. Sci. Technol. 45 (2015) 2611–2692.
- [2] N. Al Hayek, J.P. Eymery, M. Doré, Catalytic oxidation of phenols with hydrogen peroxide. Structural study by Mossbauer spectroscopy of the catalysts Fe/Al₂O₃ and FeCu/Al₂O₃, Water Res. 19 (1985) 657–666.
- [3] J.A. Botas, J.A. Melero, F. Martínez, M.I. Pariente, Assessment of Fe₂O₃/SiO₂ catalysts for the continuous treatment of phenol aqueous solutions in a fixed bed reactor, Catal. Today 149 (2010) 334–340.
- [4] M. Ferentz, M.V. Landau, R. Vidruk, M. Herskowitz, Fixed-bed catalytic wet peroxide oxidation of phenol with titania and Au/titania catalysts in dark, Catal. Today 241 (2015) 63–72.
- [5] K. Fajerwerg, J. Foussard, A. Perrard, H. Debellefontaine, Wet oxidation of phenol by hydrogen peroxide using heterogeneous catalysis Fe-ZSM-5: a promising catalyst, Water Sci. Technol. 35 (1997) 103–110.
- [6] G. Calleja, J.A. Melero, F. Martínez, R. Molina, Activity and resistance of iron-containing amorphous, zeolitic and mesostructured materials for wet peroxide oxidation of phenol, Water Res. 39 (2005) 1741–1750.
- [7] J. Barrault, M. Abdellaoui, C. Bouchoule, A.K. Majesté, J.M. Tatibouët, A. Louloudi, N. Papayannakos, N.H. Gangas, Catalytic wet peroxide oxidation over mixed (Al-Fe) pillared clays, Appl. Catal. B Environ. 27 (2000) L225–L230.
- [8] J.A. Zazo, J.A. Casas, A.F. Mohedano, J.J. Rodríguez, Catalytic wet peroxide oxidation of phenol with a Fe/active carbon catalyst, Appl. Catal. B Environ. 65 (2006) 261–268.
- [9] R.M. Liou, S.H. Chen, CuO impregnated activated carbon for catalytic wet peroxide oxidation of phenol, J. Hazard. Mater. 172 (2009) 498–506.
- [10] N. Sui, Y. Duan, X. Jiao, D. Chen, Large-scale preparation and catalytic properties of

one-dimensional α/β -MnO₂ nanostructures, *J. Phys. Chem. C* 113 (2009) 8560–8565.

[11] F. Duarte, F. Maldonado-Hódar, A. Pérez-Cadenas, L.M. Madeira, Fenton-like degradation of azo-dye Orange II catalyzed by transition metals on carbon aerogels, *Appl. Catal. B Environ.* 85 (2009) 139–147.

[12] Y. Han, N. Phonthammachai, K. Ramesh, Z. Zhong, T. White, Removing organic compounds from aqueous medium via wet peroxidation by gold catalysts, *Environ. Sci. Technol.* 42 (2008) 908–912.

[13] S. Navalón, A. Dhakshinamoorthy, M. Alvaro, H. García, Heterogeneous Fenton catalysts based on activated carbon and related materials, *ChemSusChem* 4 (2011) 1712–1730.

[14] C.M. Dominguez, P. Ocón, A. Quintanilla, J.A. Casas, J.J. Rodriguez, Graphite and carbon black materials as catalysts for wet peroxide oxidation, *Appl. Catal. B Environ.* 144 (2014) 599–606.

[15] C.M. Dominguez, A. Quintanilla, J.A. Casas, J.J. Rodriguez, Kinetics of wet peroxide oxidation of phenol with a gold/activated carbon catalyst, *Chem. Eng. J.* 253 (2014) 486–492.

[16] O.P. Taran, A.N. Zagoruiko, A.B. Ayusheev, S.A. Yashnik, R.V. Prihod'ko, Z.R. Ismagilov, V.V. Goncharuk, V.N. Parmon, Wet peroxide oxidation of phenol over Cu-ZSM-5 catalyst in a flow reactor. Kinetics and diffusion study, *Chem. Eng. J.* 282 (2015) 108–115.

[17] X. Zhou, C.-J. Liu, Three-Dimensional printing for catalytic applications: current Status and perspectives, *Adv. Funct. Mater.* 27 (2017) 1701134.

[18] R.D. Farahani, M. Dubé, D. Therriault, Three-dimensional printing of multi-functional nanocomposites: manufacturing techniques and applications, *Adv. Mater.* 28 (2016) 5794–5821.

[19] J.E. Smay, G.M. Gratson, R.F. Shepherd, J. Cesarano III, J.A. Lewis, Directed colloidal assembly of 3D periodic structures, *Adv. Mater.* 14 (2002) 1279–1283.

[20] J.N. Stuecker, J.E. Miller, R.E. Ferrizz, J.E. Mudd, J. Cesarano III, Advanced support structures for enhanced catalytic activity, *Ind. Eng. Chem. Res.* 43 (2004) 51–55.

[22] C.R. Tubío, J. Azuaje, L. Escalante, A. Coelho, F. Gutián, E. Sotelo, A. Gil, 3D printing of a heterogeneous copper-based catalyst, *J. Catal.* 334 (2016) 110–115.

[23] J.H. Eom, Y.W. Kim, S.J. Raju, Processing and properties of macroporous silicon carbide ceramics: a review, *Asian Ceram. Soc.* 1 (2013) 220–242.

[24] G. Roewer, U. Herzog, K. Trommer, E. Müller, S. Fröhlauf, Silicon-carbide- a survey of synthetic approaches, properties and applications, *Struct. Bond.* 101 (2002) 59–135.

[25] M.J. Ledoux, C. Pham-Huu, Silicon carbide: a novel catalyst support for heterogeneous catalysis, *CATTECH* 5 (2001) 226–246.

[26] E.V. Rokhina, J. Virkutyte, Environmental application of catalytic processes: heterogeneous liquid phase oxidation of phenol with hydrogen peroxide, *Crit. Rev. Environ. Sci. Technol.* 41 (2011) 125–167.

[27] B. Román-Manso, A. de Pablos, M. Belmonte, M.I. Osendi, P. Miranzo, Microstructural designs of spark plasma sintered silicon carbide ceramic scaffolds, *Bol. Soc. Esp. Ceram. Vidr.* 53 (2014) 93–100.

[28] T. Yamashita, P. Hayes, Effect of curve fitting parameters on quantitative analysis of Fe_{0.94}O and Fe₂O₃ using XPSJ, *Electron. Spectrosc. Relat. Phenom.* 152 (2006) 6–11.

[29] S. Wang, Comparative study of Fenton and Fenton-like reaction kinetics in decolorisation of wastewater, *Dyes Pigm.* 76 (2008) 714–720.

[30] A. Santos, P. Yustos, S. Rodríguez, A. Romero, Mineralization lumping kinetic model for abatement of organic pollutants using Fenton's reagent, *Catal. Today* 151 (2010) 89–93.

[31] M. Vallejo, M. Fresnedo San Román, I. Ortiz, A. Irabien, The critical role of the operating conditions on the Fenton oxidation of 2-chlorophenol: assessment of PCDD/Fs formation, *J. Hazard. Mater.* 279 (2014) 579–585.

[32] J. Carabao, A. Quintanilla, J.A. Casas, Assessment of carbon monoxide formation in Fenton process: the critical role of pollutant nature and operating conditions, *Appl. Catal. B Environ.* 232 (2018) 55–59.

[33] J.L. Diaz de Tuesta, A. Quintanilla, J.A. Casas, J.J. Rodriguez, Kinetic modeling of wet peroxide oxidation with a carbon black catalyst, *Appl. Catal. B Environ.* 209 (2017) 701–710.

[34] C.M. Dominguez, P. Ocón, A. Quintanilla, J.A. Casas, J.J. Rodriguez, Highly efficient application of activated carbon as catalyst for wet peroxide oxidation, *Appl. Catal. B Environ.* 140/141 (2013) 663–670.

[35] M.T. Kreutzer, F. Kapteijn, J.A. Moulijn, J.J. Heiszwolf, Multiphase monolith reactors: chemical reaction engineering of segmented flow in microchannels, *Chem. Eng. Sci.* 60 (2005) 5895–5916.

[36] K.M. Valkaj, A. Katovic, S. Žrnčević, Investigation of the catalytic wet peroxide oxidation of phenol over different types of Cu/ZSM-5 catalyst, *J. Hazard. Mater.* 144 (2007) 663–667.

[37] V. Subbaramaiah, V.Ch. Srivastava, I.D. Mall, Optimization of reaction parameters and kinetic modeling of catalytic wet peroxidation of picoline by Cu/SBA-15, *Ind. Eng. Chem. Res.* 52 (2013) 9021–9029.

[38] C.R. Wilke, P. Chang, Correlation of diffusion coefficients in dilute solutions, *AIChE J.* 1 (1995) 264–279.

Further reading

[21] J. Azuaje, C.R. Tubío, L. Escalante, M. Gómez, F. Gutián, A. Coelho, O. Caamaño, A. Gil, E. Sotelo, *Appl. Catal. A Gen.* (530) (2017) 203–210.